Influence of bottom topography on large-scale decadal basin modes

by Dhouha Ferjani[1,2], Thierry Huck[1] and Alain Colin de Verdière[1]

ABSTRACT

The influence of bottom topography on the generic properties of the baroclinic basin modes is investigated through linear stability analysis of a two-layer shallow water ocean model. Various idealized bottom profiles imitating a mid-ocean ridge and continental slopes are analyzed in an extratropical β-plane closed basin. Only large-scale features are examined, the eddy effects being parametrized as turbulent eddy viscosity that allows the selection of large-scale eigenmodes. At coarse resolution, the largest-scale lowest-frequency baroclinic modes appear as the least damped modes. For scales much larger than the internal deformation radius, the damping rate is relatively independent of dissipation, the mode energy—mostly potential—being depleted by lateral dissipation work. The damping rate of the leading baroclinic mode is found to be weakly sensitive to bottom topography, while the decadal period is shortened by bottom undulations. The mechanism of modal decay is rationalized through energy and vorticity budgets for the barotropic and baroclinic components, to characterize the energy routes and conversions. For small amplitude topography, the barotropic flow results accurately from the interaction of the flat-bottomed baroclinic motion with the topographic height: it is found to be three times stronger within closed potential vorticity contours than with blocked contours. However, the conversion of energy from the baroclinic to the barotropic mode remains weaker than the frictional processes.

1. Introduction

The effects of anthropogenically-forced climate change are expected to continue through the 21st century and beyond (Solomon et al. 2011). On timescales of a few years to a few decades, future regional changes in weather patterns and climate and the corresponding impacts will also be strongly influenced by natural climate variations driven by the Atlantic thermohaline circulation (Delworth et al. 2006). On interdecadal timescales, the existence of this intrinsic climate variability known as the Atlantic Multidecadal Oscillation (Kerr 2000) has been demonstrated by numerous analysis of historical and climatological time series, and in a broad range of ocean models. All these studies aim to better understand

1. Laboratoire de Physique des Océans, Université de Bretagne Occidentale, UFR Sciences, 6 avenue Le Gorgeu, BP 809, 29285 Brest cedex, France.
2. Corresponding author *e-mail: dhouha.ferjani@univ-brest.fr*

how the atmosphere or ocean varies on its own, under either thermodynamic or mechanical forcing imposed by its counterpart, which is not a small issue regarding the wide range of temporal and spatial scales and diverse physical phenomena.

The low-frequency ocean circulation is likely a major player, given its large heat capacity and long adjustment. The latter is achieved through the baroclinic planetary waves that cross the Atlantic basin in a few decades at mid-latitude. The baroclinic Rossby basin modes have thus been proposed as a possible explanation for these variability signals: they are westward-propagating Rossby waves reinitiated at the eastern boundary through rapid Kelvin wave adjustment (LaCasce 2000) or nonresonant inertia-gravity wave response (Primeau 2002), and owe their existence to mass conservation laws (Cessi and Primeau 2001). Their damping rate is independent of friction when Rossby wave velocity depends on latitude, as in the shallow water equations (Cessi and Louazel 2001).

Most of these studies examined the low-frequency large-scale basin modes as prototypes for interdecadal oscillation from a quasigeostrophic point of view. Nonetheless, all of them considered a flat bottom or a reduced gravity configuration so the effect of topography could be ignored. For instance, several studies have explored the baroclinic response to wind-forced circulation with idealized models. LaCasce (2000) and Cessi and Primeau (2001) examined it in a different parameter range and with a square basin, while Primeau (2002) and LaCasce and Pedlosky (2002) looked at baroclinic waves in closed basins, considering also shallow water equations and irregular geometry. Spydell and Cessi (2003) together with Ben Jelloul and Huck (2005) studied the time-dependent circulation in a closed basin where the mean flow is specified. Specifically, they examined the large-scale baroclinic eigenmodes of a two-layer rectangular basin over a flat bottom with a quasigeostrophic model forced by surface wind stress.

It is then natural to wonder what effect the removal of these simplifications (quasigeostrophy, flat-bottom) might have on the structure of the baroclinic basin modes, given the well-known tendency of the large-scale topography to couple the vertical modes. The importance of bottom topography for the dynamics of the ocean has been pointed out by many authors (e.g. Rhines 1969a,b; Ripa 1978; Mertz and Wright 1992). A baroclinic current flowing over sloping bottom topography on the rotating solid earth can generate a barotropic flow by releasing the available potential energy, a concept established by Sarkisyan and Ivanov (1971) and called JEBAR (Joint Effect of Baroclinicity and Relief). This approach has been a powerful tool to explain some fundamental mechanisms in the ocean circulation such as the Gulf Stream transport magnitude and separation (e.g. Mellor et al. 1982). A comprehensive description in the review of Rhines (1977) of the geostrophic turbulence cascade first in a free configuration then in the presence of coastal boundaries and bottom topography stresses the competition between the turbulent behavior and wave dynamics in a flat-bottomed, homogeneous ocean creating a tendency to zonally elongated bands of barotropic flow. The main effect of topographic roughness found in the quasigeostrophic numerical experiments of free-decaying turbulence is a stabilization of the baroclinic modes against the energy loss due to the nonlinear energy transfer into the barotropic mode. In a

related study, Böning (1989) highlighted similar results using an eddy-resolving circulation model, both driven by a steady zonal wind stress and by heat fluxes. Specifically, he argued that the interactions of the deep current fluctuations with the synoptic-scale irregularities of the ocean floor enhance the baroclinicity of the eddy field, whereas a strong tendency toward barotropization is revealed in a flat-bottom solution.

The numerical solution of Barnier (1988) shows that free baroclinic Rossby waves can be generated in the ocean interior by the wind or by an ocean ridge. In Tailleux and McWilliams (2000), a freely propagating baroclinic eddy is depleted while propagating over a ridge as a result of topographic coupling with the barotropic mode, suggesting that the energy transfer can also occur in the opposite direction (i.e. from the baroclinic to the barotropic mode).

Winton (1997) investigated the qualitative effect of sidewall topography upon internal decadal oscillations of the thermocline circulation, and showed its damping influence by comparison with the response of the flat bottom experiment.

This study is motivated by the desire to pursue these investigations by considering the influence of different finite-amplitude topographic features on the generic property of the decadal oscillations as well as their damping. Specific questions of interest are: 1). What drives the barotropic circulation in the linear regime in the absence of external forcing?; 2). What causes the damping of the low-frequency and large-scale baroclinic modes and does the topography modify the baroclinic geostrophic adjustment time-scale? If so, in what manner? To consider finite amplitude topography a shallow water model is needed. We use here a two-layer shallow water model on top of various idealized bottom topography (bowl, ridge) in order to characterize the large-scale, wavelike response in a closed ocean basin. This model formulation allows also for a latitudinal variation of the Rossby radius which is critical for the decadal variability of the ocean circulation. We have chosen to focus on the large-scale regime and keep explicit mesoscale eddy resolution for later work.

We investigated the above issues through vorticity and energy budgets, considering their vertical partition into barotropic and baroclinic modes. The material is organized as follows: the model and configuration are presented in Section 2, vorticity and energy budgets are described in detail in Section 3 and 4. Section 5 discusses the parametrization of unresolved processes and Section 6 provides some conclusions.

2. Formulation and model description

We describe the model based on the two-layer shallow water (SW) equations with explicit dissipation but no external forcing, and perform a linear stability analysis to extract the pure baroclinic basin modes interacting with a specified bottom topography.

a. Two-layer SW equations

A simple theoretical model is constructed to address the effect of topography on unforced modes. We seek insight into the mechanisms associated with the propagation and decay of baroclinic planetary modes in the presence of large-scale bottom topography. The
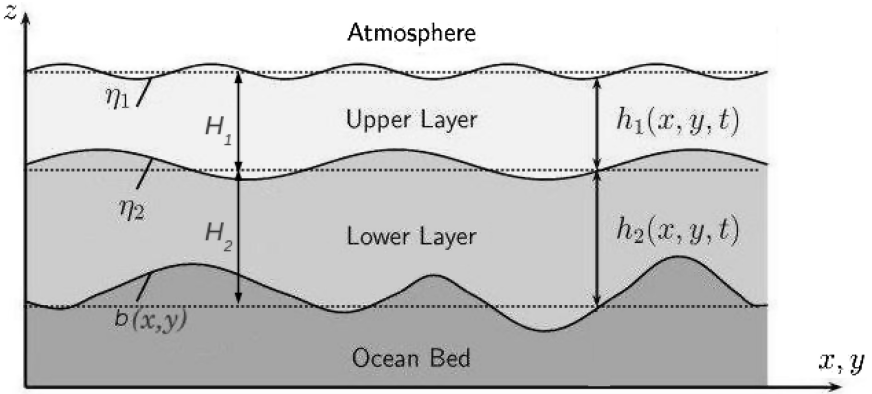
Figure 1. Schematic structure of the two-layer ocean model and notations.

applicability of quasigeostrophic models of β-plane oceans to such a study is limited, however, because on larger scales both the basic stratification and the topography have large amplitude variations, in which the continuous stratification in the real ocean is modeled, hereafter as two immiscible, vertically homogeneous layers.

The enclosed Cartesian β-plane ocean basin $D = \{0 \leq x \leq L_x, -L_y/2 \leq y \leq L_y/2\}$ is centered at 45°N, extending from 15°N to 75°N and of 60° in longitude. The Coriolis parameter f is linearized about a reference latitude so that $f = f_0 + \beta y$, and β its latitudinal derivative, is constant (β-plane approximation). In the absence of external forcing, the equations of motion are:

$$D_t \mathbf{u_i} + f\mathbf{k} \times \mathbf{u_i} = -\nabla \left(g\eta_1 + \delta_{i2}g'(\eta_2 - \eta_1) \right) + \nu\nabla^2 \mathbf{u_i}, \tag{1a}$$

$$\partial_t h_i + \nabla \cdot (h_i \mathbf{u_i}) = 0. \tag{1b}$$

The notation is standard, i.e. h_i, $\mathbf{u_i}$ denote the thickness and velocity of each layer $i = 1, 2$ and compose the state vector that we have to solve for. The unit vector $\mathbf{k}$ points upward, δ_{ij} the Kronecker delta operator, ρ_i the density in each layer, g the acceleration due to gravity and $g' = g\frac{\rho_2-\rho_1}{\rho_2}$ the reduced gravity. The dissipation in each layer is represented by a horizontal Laplacian friction using ν as lateral eddy viscosity.

We denote by η_1 the free surface elevation and η_2 the interface displacement with respect to undisturbed reference levels H_i. They are related to the total layer thicknesses by $h_1 = H_1 + \eta_1 - \eta_2$ and $h_2 = H_2 + \eta_2 - b$, such that $h(x, y, t) = h_1 + h_2 = H_0 + \eta_1(x, y, t) - b(x, y)$ corresponds to the total fluid layer thickness, with $H_0 = H_1 + H_2$ being the constant undisturbed fluid thickness (Figure 1). The bottom topography $b(x, y)$ is measured from the level surface lying at the bottom of the second layer.

For small disturbances to a stratified motionless background state, the linearized version of (1) is obtained for the perturbation thickness $h_1' = \eta_1' - \eta_2'$ and $h_2' = \eta_2'$:

Table 1. Typical parameters for the experiment in the linear shallow-water model.

Symbol	Value	Description
f_0	$10^{-4}\,\text{s}^{-1}$	Coriolis parameter at $y = 0$ (45°N)
β	$1.6\,10^{-11}\,\text{m}^{-1}\,\text{s}^{-1}$	Meridional gradient of Coriolis parameter
L_x	6600 km	Basin zonal extent
L_y	6600 km	Basin meridional extent
H_1	1000 m	Upper layer mean depth at rest
H_2	3000 m	Bottom layer mean depth at rest
H_0	$H_1 + H_2$	Total mean depth at rest
ρ_0	$1023\,\text{kg m}^{-3}$	Mean density
g	$9.81\,\text{m s}^{-2}$	Gravity acceleration at Earth surface
$g' = g\Delta\rho/\rho$	$0.02\,\text{m s}^{-2}$	Reduced gravity acceleration
ν	$10^5\,\text{m}^2\text{s}^{-1}$	Laplacian eddy viscosity
$n_x \times n_y$	60×60	Number of grid points in the horizontal

$$\partial_t \mathbf{u'_i} + f\mathbf{k} \times \mathbf{u'_i} = -\nabla\left(g(h'_1 + h'_2) - \delta_{i2}g'h'_1\right) + \nu\nabla^2\mathbf{u'_i}, \tag{2a}$$

$$\partial_t h'_i + \nabla \cdot \left[(H_i - \delta_{i2}b)\mathbf{u'_i}\right] = 0. \tag{2b}$$

In the following, the primes are dropped for convenience. The appropriate internal deformation radius for baroclinic modes over a flat bottom $R_d(y) = \sqrt{g'H_e}/f$, where $H_e = H_1H_2/H_0$ is the equivalent depth, depends on latitude. Using typical parameter values, $R_d = O(40\,\text{km})$ at midlatitudes and the corresponding long-wave limit of the baroclinic Rossby wave westward velocity $c = \beta R_d^2$ is then a few 10^{-2} m s^{-1}, leading to a decadal scale basin crossing time (depending upon latitude).

No-slip boundary conditions are imposed on the lateral solid walls, i.e. $\mathbf{u} \cdot \mathbf{n} = 0$, with $\mathbf{n}$ the vector normal to the boundaries, to ensure mass conservation.

The approach of Huck et al. (1999) is used to parametrize the horizontal flux of momentum due to the mesoscale eddies with a Laplacian friction closure. This form of dissipation is enforced here as a filter to select large-scale modes through their lowest damping rate (Huck and Vallis, 2001).

Given the horizontal resolution Δx large compared to the oceanic internal Rossby radius, we follow current practice to determine the viscosity coefficient as a function of the horizontal resolution $\nu > 1.6\,\beta\Delta x^3$ (m^2 s^{-1}) to insure that the model correctly resolves Munk's boundary layer $\delta_M = (\nu/\beta)^{1/3}$. The implied horizontal mixing of momentum is then much larger than expected or estimated from eddy processes, and the actual western boundary currents remain in a viscous regime in the present model. Although the friction coefficient is large, interior flows of scale L are geostrophic to order ν/fL^2, a ratio of friction to Coriolis terms. For L of order 1,000 km, this ratio is less than 1% for the values used here. Such values along with those appended in Table 1 are within the observational range and used as pivots around, which other regimes are explored.
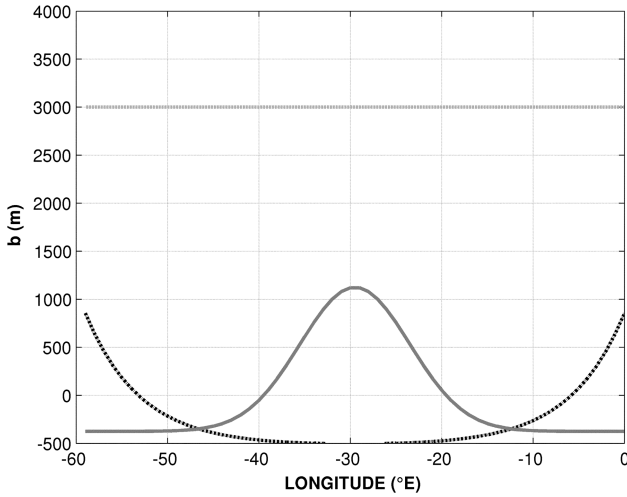
Figure 2. Analytical bottom topography profiles corresponding to 1,500 m amplitude height (MOR dashed, CR dash-dotted). The dashed line denotes the interface level at rest measured from the bottom mean depth.

Sensitivity tests to the form and height of the topographic features are carried out by implementing two idealized bottom profiles (Figure 2) along with quantitative comparisons with the flat bottom experiment. The first experiment implements a gaussian shape Mid-Ocean Ridge (MOR) in the x-direction, centered in the middle of the basin, that we expect to disturb Rossby waves westward propagation. Such a simple approach offers the ability to assess the sensitivity of the solutions to parametrizations of unresolved processes. The second experiment implements a gently sloping bowl-shaped topography, called Continental Rises (CR). In all cases, the *e*-folding scale of the bottom elevation is around one third of the basin zonal extent with a height spanning from 0 to 2,500 m. The bottom depth is adjusted such that the basin volume remains constant.

b. Linear stability analysis

The principle of the linear stability analysis used herein to find out the wave modes is to examine the evolution of a small perturbation about a steady state, taken here at rest. The linearized prognostic equations (2) of the model can be written as a general dynamical system:

$$\partial_t X = J X, \tag{3}$$

where J is the Jacobian matrix and $X = (h_i, \mathbf{u}_i)$ is the state vector. Assuming that the solution has a wave-like form:

$$X = \begin{bmatrix} h_i \\ \mathbf{u_i} \end{bmatrix}(x,\ y,\ t) = e^{\omega t} \begin{bmatrix} \hat{h}_i \\ \hat{\mathbf{u}}_i \end{bmatrix}(x,\ y), \tag{4}$$

the eigenvalue problem of the perturbations simply reads $\omega X = J X$, with ω the eigenvalue and J the nonsymmetric Jacobian matrix. Two methods have been implemented, one based on the explicit Jacobian of the model, the other on the linear tangent model. In the first case, the Jacobian matrix of the linear system is explicitly computed from the finite differ-ence formulation of the equations on an regular Arakawa C-grid with a 60-point standard resolution in each direction. Its leading eigenvalues (typically 30) based on the largest real part are computed using Arnoldi's method as provided in ARPACK (Lehoucq et al. 1996). This method is limited by the size of the explicit Jacobian matrix. In the second case, the tangent linear model is used to compute the leading eigenvalues of the propagator $M(\tau)$ over a 'short' integration time ($\tau = 0.1$ yr here) with ARPACK:

$$X(t = \tau) = M(\tau) X(t = 0) = e^{J\tau} X(t = 0), \tag{5}$$

where the initial perturbations $X(t = 0)$ are provided by the Arnoldi method. The same spatial discretization is used with centered second-order advection and diffusion schemes, whereas the temporal scheme is second-order with an Asselin time filter. The Jacobian eigenvalues ω are then computed from the propagator eigenvalues $e^{\omega\tau}$. We have checked that the results are not sensitive to the integration time τ over a large range of values, small compared to the baroclinic Rossby basin crossing time, but large with respect to the gravity waves basin crossing time. This latter method is much more efficient, and avoids the computation of the explicit Jacobian matrix, hence allowing a much larger number of model grid points (up to 300 in each direction).

Unless otherwise specified, our solutions are obtained in an idealized basin with the typical parameters listed in Table 1. Solutions are extremely stable with the horizontal resolution, with variations of a few percent in eigenvalues. We perform the linear stability analyses for the flat-bottom case and the two forms of bottom topography with increasing amplitudes. In all cases, the eigenvalues display a negative real part (stable damped modes) with several ones having a rather small negative real part, hence representing weakly damped modes on time scales of decades. In the following, we examine the characteristics of the least damped basin modes that have large spatial scale and decadal timescale as function of the bottom shape and height. Table 2 gives the eigenvalues of the two least damped modes and Figure 3 shows the patterns of the gravest mode.

Since the physical model solution must be real, the complex conjugate eigenvalues ($\omega_r \pm i\omega_i$) are associated with complex conjugate eigenvectors ($V_r \pm i V_i$). Letting aside the damping rate, which only modulates the amplitude of the oscillation, the time evolution due to the imaginary part of the eigenvalue follows:

$$X(t) = X_r \cos(\omega_i t) - X_i \sin(\omega_i t), \tag{6}$$

which yields a temporal sequence $X_r \to -X_i \to -X_r \to X_i$ every quarter period for a positive ω_i. The real and imaginary parts of the least damped basin mode eigenvalue of the topographic experiments show slight changes by about 10 to 15% compared with that of

Table 2. First two eigenvalues of the tangent linear model matrix under three different topographic features: flat, meridional ridge and continental rises. The damping time scale is defined as $\tau = 1/\omega_r$ and the oscillation period $T = 2\pi/\omega_i$.

	Mode	ω_r (yr^{-1})	ω_i (yr^{-1})	τ (yr)	T (yr)	τ/T
Flat case	1	−0.2025	0.3652	−4.93	17.21	0.2860
	2	−0.2867	0.7370	−3.48	8.52	0.4080
1500 m-MOR case	1	−0.2276	0.4261	−4.39	14.74	0.2970
	2	−0.3273	0.7483	−3.05	8.39	0.3635
1500 m-CR case	1	−0.2177	0.4471	−4.59	14.05	0.3260
	2	−0.2260	0.9060	−4.42	6.93	0.6370

the flat bottom experiment. A large scale pattern intensified in the north-west quarter of the domain characterizes the three experiments (flat, mid-ocean ridge and continental slopes). Figure 3 displays the spatial structure of the least damped mode in the case of 2,500 m bottom height experiment compared with the flat bottom case. In this steep topography limit, the topographic β effect $f \nabla h/h$ is greater than the planetary β, yet the spatial structure shows minor changes compared to the flat-bottomed baroclinic mode. The propagation of long Rossby waves remains westward and nondispersive as in the flat-bottom case, evidencing the robustness of planetary modes to topographic features. The propagation with Hovmöller diagrams (i.e. longitude-time plots) sketched in Figure 4 confirms this statement and shows a rather regular pattern of westward propagating waves with a phase tilt consistent with the long baroclinic Rossby phase speed c of 2.57×10^{-2} m s^{-1} at 30°N. A comparatively strong signal compared to the interior is also trapped in a thin Munk-type western boundary layer.

In the presence of topography, the differences with the flat bottom propagation are three-fold: 1). an amplification of the oscillation amplitude over the bottom relief; 2). a shortening of the oscillation period revealing an enhancement of the propagation speed in agreement with Tailleux and McWilliams (2000) and; 3). a strengthening of the oscillation damping rate. With continental slopes, the baroclinic mode appears relatively less damped with a shorter propagation period and a longer decay time with respect to the mid-ocean ridge mode.

3. Linear vorticity balance

Apart from frictional interaction with the boundaries, losses from baroclinic flow to barotropic dynamics take place when both topography and stratification are present, although the rates and mechanisms by which this occurs are uncertain. The resolution of this issue is however essential for the advancement of modeling parametrizations. In order to better understand how the barotropic mode is built-up by the interaction of the
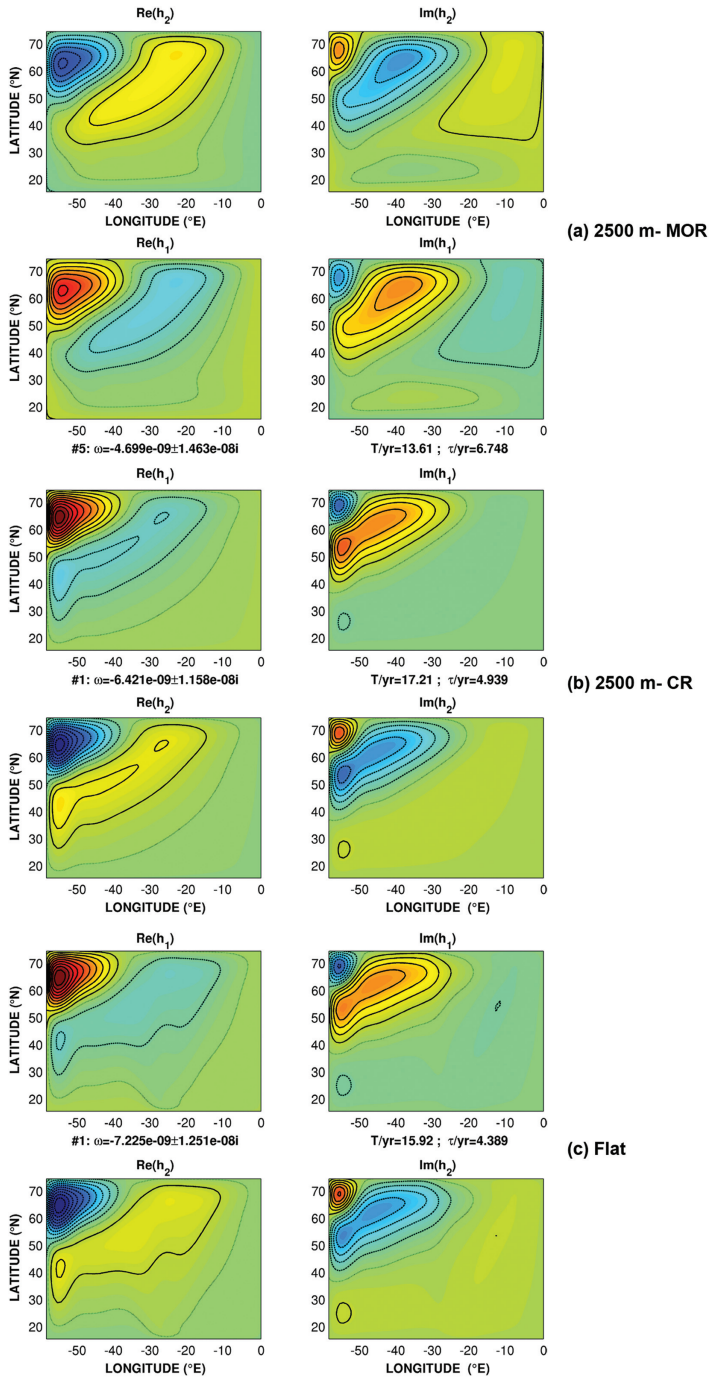
Figure 3. Real parts (left) and imaginary parts (right) of the least damped eigenvector for the upper and bottom layer thickness anomalies in the presence of different bottom profiles. The mode amplitude is arbitrary. Negative (positive) contours are dashed (solid) and the zero contour is dotted.
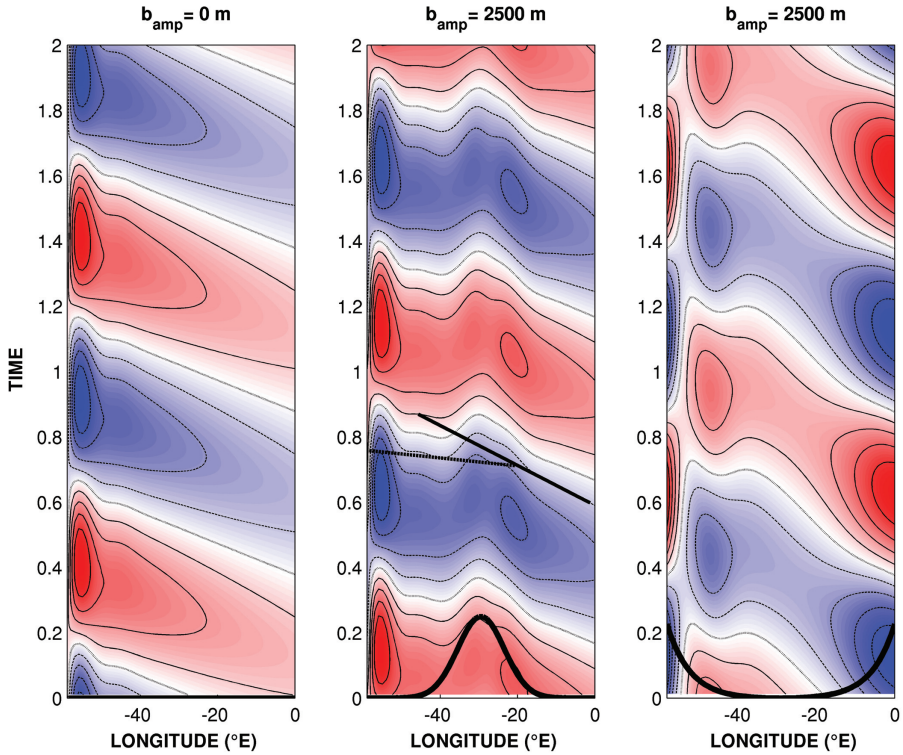
Figure 4. Hovmöller diagrams at 30°N for the sea level anomaly of the non-decaying propagating least damped basin mode in the presence of a flat bottom, a ridge (MOR) and continental slopes (CR). Superimposed are straight lines for the standard phase speed (solid) and enhanced phase speed west of the topographic obstacle (dashed). The overlaid arbitrary heights of the bottom are drawn to indicate the correlation with the changes in the propagation speed. Time is scaled by the period of the flat-bottomed least damped mode.

baroclinic mode with the topographic constraint, the vorticity equation for the vertically averaged flow is examined. For each variable, we note X^+ the vertically averaged component defined as $hX^+ = h_1 X_1 + h_2 X_2$, and $X^- = X_1 - X_2$ its baroclinic counterpart (so that $X_1 = X^+ + \frac{h_2}{h} X^-$ and $X_2 = X^+ - \frac{h_1}{h} X^-$). Vertical integration of the linear momentum balance (2a) provides the equation for the horizontal transport $(h\mathbf{u}^+)$:

$$\partial_t (h\mathbf{u}^+) + f\mathbf{k} \times (h\mathbf{u}^+) = -H_0 \nabla p^+ + b\nabla p_2 + F, \qquad (7)$$

where the vertical integration of the pressure term can be decomposed as barotropic pressure and bottom pressure, and F is the vertical integral of lateral friction.

The linear vorticity equation follows by taking the curl of (7):

$$\partial_t \zeta^+ = -f\nabla \cdot (h\mathbf{u}^+) - \beta h v^+ + J(b, p_2) + \mathbf{k} \cdot \nabla \times F. \qquad (8)$$

This equation expresses the fact that the local rate-of-change of the vertically integrated vorticity is caused by the planetary vorticity tendency, the effect of the bottom pressure torque, curl $(b\nabla p_2)$, and lateral friction torque. The detailed derivation of (8) is given in Appendix A. Here $\zeta^+ = \partial_x(hv^+) - \partial_y(hu^+)$ is the relative vorticity of the vertically integrated transport; $J(b, p_2)$ represents the Jacobian of the bottom height and the bottom layer pressure, referred to as the JEBAR term (Mertz and Wright 1992). For large scale solutions slowly varying in time, the horizontal velocity is in geostrophic equilibrium. In the lower layer, the (geostrophically balanced) Eulerian velocity $\mathbf{u}_2^{\mathbf{G}}$ is related to the bottom pressure torque $-f\mathbf{u}_2^{\mathbf{G}}\nabla b = J(b, p_2)$. Further manipulating this term with respect to the barotropic and baroclinic components of the flow $\mathbf{u}_2^{\mathbf{G}} = \mathbf{u}^+ - \frac{h_1}{h}\mathbf{u}^-$, and making use of the depth-integrated continuity equation gives:

$$\partial_t\zeta^+ = f\,\partial_t\eta_1 - \beta h v^+ - f\mathbf{u}^+\nabla b + \frac{H_1}{h}J(p^-, b) + \mathbf{k}\cdot\nabla\times F. \tag{9}$$

Equation 9 is the form of the linear vorticity equation obtained by enforcing the free surface pressure formulation instead of the often-used rigid lid approximation. Time derivatives are $O(10^{-2})$ compared to the other terms, while the friction is only relevant in the western boundary layer, they can then be safely neglected in (9), which finally reduces to:

$$J\left(\psi^+, \frac{f}{h}\right) = \frac{H_1}{h^2}J(p^-, b). \tag{10}$$

This form of linear vorticity equation is appealing because it makes explicit the concept that the bottom pressure torque (or JEBAR effect) forces the barotropic transport across f/h contours. It is obtained by assuming the nondivergence of the vertically-integrated horizontal transport $\mathbf{k}\times\nabla\psi^+ = h\mathbf{u}^+$. The extent to which the generated barotropic circulation is sensitive to bottom topography depends crucially on the bottom height. We verify this result analytically by considering the topography as a small perturbation over a flat bottom $h = H_0$ so that $\epsilon = b/H_0 \ll O(1)$ and solve (10) by a weakly nonlinear expansion in power of ϵ for ψ^+, p^- and b:

$$\psi^+ = \psi_0^+ + \epsilon\,\psi_1^+ + \epsilon^2\,\psi_2^+ + \dots,$$
$$p^- = p_0^- + \epsilon\,p_1^- + \epsilon^2\,p_2^- + \dots,$$
$$b = b_0 + \epsilon\,b_1 + \epsilon^2\,b_2 + \dots,$$

where p_0^- represents the baroclinic pressure of the purely baroclinic flow ($\psi_0^+ = 0$) over the flat bottom ($b_0 = 0$). At first order, (10) becomes:

$$\beta\partial_x\psi_1^+ = \frac{H_1}{H_0}J(p_0^-, b_1), \tag{11}$$

This is a Sverdrup type equation that can be integrated from the eastern boundary where the normal component of the velocity vanishes at the east coast ($\psi^+ = 0$).

From (11), it is then obvious that the barotropic mode vanishes with vanishing topography. The governing equation (11) together with the boundary condition form a well-posed system away from the western boundary. The barotropic transport streamfunction is now determined diagnostically and compared to the one derived from the barotropic transport (Ψ^+) of the actual solution with variable topography.

For a bottom height up to 1,000 m ($\epsilon = 0.125$), the two large-scale patterns related to the interior planetary geostrophic approximation and the full problem display strong agreement (rms<11%), despite some discrepancies near the western boundary layer where the friction—not considered in (11)—becomes important. Only the case of a 500 m CR-experiment is shown in Figure 5 but the same conclusion holds for the MOR-experiment: the barotropic mode is accurately diagnosed through the interaction of the flat-bottomed baroclinic mode with the imposed topography elevation.

The spatial distribution of the approximated barotropic streamfunction is examined in the case of a meridional mid-ocean ridge (Figure 6). When the baroclinic flow ascends the eastern flank of the ridge, the JEBAR term generates positive vorticity at the northern half of the ridge. This vorticity input allows barotropic currents to cross the PV contours, instead of just following them. The opposite process happens when the flow travels farther over the western flank of the ridge. Accordingly, a barotropic cyclonic gyre is generated over the ridge together with an anticyclonic gyre just to the south. The barotropic structure obtained in the north-west corner produces an eastward jet under the effect of only the JEBAR term, in a way similar to the classical wind-driven double gyre structure (Holland 1978; among many others). A similar argument holds for the case of a bowl-shaped topography where the western half of the ridge is equivalent to the eastern continental slope. Notice that the orientation of the generated barotropic jet is defined by the perturbation sign. That is for an opposite-sign perturbation, the barotropic jet would point westward. This situation is similar to the strong jetlike current formation between two opposite sign eddies under the interaction of a current with a seamount (Verron and Le Provost 1985; Herbette et al. 2003).

4. Mechanisms of modal decay

The consideration of energetics is essential to establish the mechanism of modal decay. This mechanism has been elegantly tackled by Cessi and Louazel (2001) in the case of a reduced gravity basin. They found the decay rate to be independent of friction as long as the latter remains weak, and uniquely established by the difference between the slowest and fastest long Rossby wave speeds in the inviscid limit. The damping arises through the tilting of the wavefronts by the latitudinal variations of Rossby waves phase speed that get partially absorbed on the western boundary. This case is considered as the simplest although enlightening model: the energy balance of the baroclinic mode consists of a predominant reservoir of available potential energy *APE* (of order $(L_x/R_d)^2$ times the kinetic energy in the large-scale ocean circulation, (Gill et al. 1974)) converted into eddy kinetic
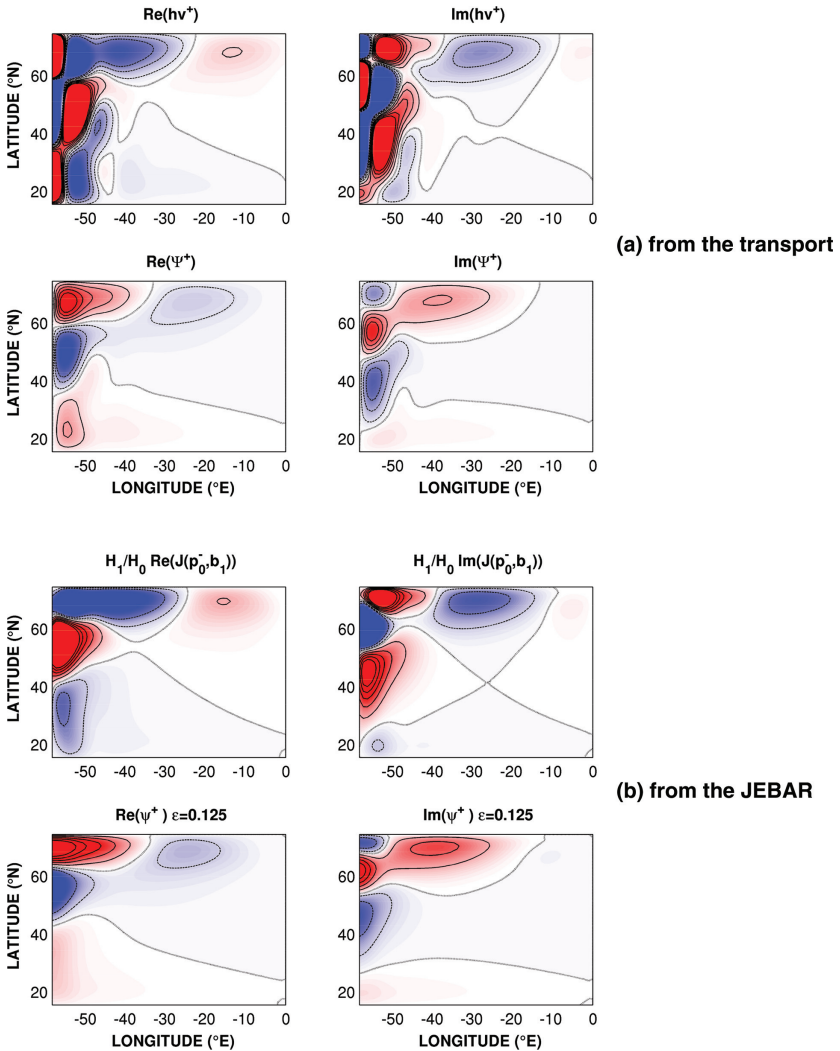
Figure 5. Real parts (left) and imaginary (right) parts of the barotropic transport streamfunction in the CR-experiment: a). as obtained from the vertically integrated horizontal transport (upper panel) and b). diagnostically calculated using the JEBAR term in Equation (11) (bottom panel). A weak topography amplitude $\epsilon = 0.125$ is used. Note the approximated solution b). does not resolve the western boundary current, so no good agreement is expected there.

energy *EKE* and dissipated by linear friction. The damping time scale ω_r is simply the ratio $-2r\,EKE/APE$, in which r is the linear drag coefficient. However, in our calculations, the problem is a little more complicated, as it also takes into account the interaction of the two active layers with a realistic bottom topography. Hence, apart from the Laplacian

t=0.17   **t=0.33**   **t=0.5**

t=0.67   **t=0.83**   **t=1**

LATITUDE (°N)

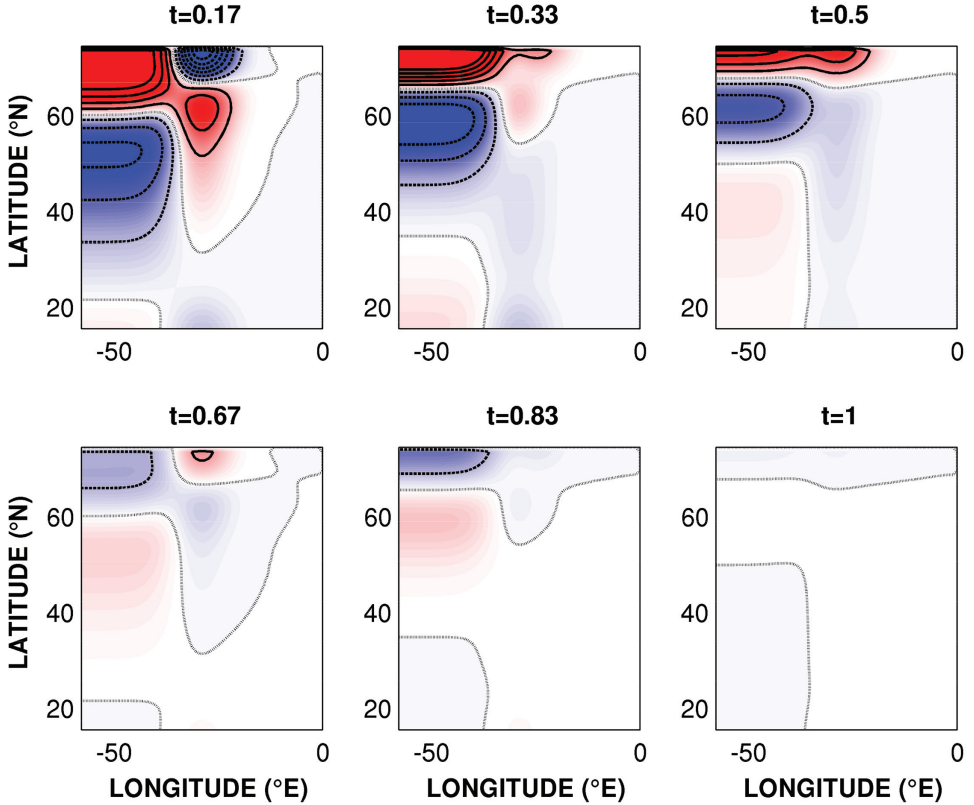**LONGITUDE (°E)**   **LONGITUDE (°E)**   **LONGITUDE (°E)**

Figure 6. Barotropic transport streamfunction derived from (10) in the 500 m-MOR experiment as a function of time for one oscillation cycle. The region of negative values are in blue and positive values are in red.. Time is scaled by the period of the flat-bottomed least damped mode. Around half the oscillation cycle, the generated barotropic perturbation is strongly weakened by viscous processes.

viscous dissipation that we include to neutralize short scale instabilities, the modal decay is expected to be conditioned also by the effect of bottom variations.

Before calculating the energy generation/dissipation terms, we present the formulation of the vertical mode partition of the total energy of the model. Multiplying the vertically integrated momentum equation (7) by $\mathbf{u}^+$ gives the temporal evolution of the barotropic energy (details of the calculation can be found in Appendix B):

$$\frac{1}{2}h\partial_t|\mathbf{u}^+|^2 + \frac{1}{2}g\partial_t\eta_1^2 = -\nabla\cdot(h\,p^+\mathbf{u}^+) + \frac{h_2}{h}p^-\partial_t\eta_1 + p^-\mathbf{u}^+\frac{H_1}{h}\nabla b + LF^+. \quad (12)$$

Similarly, subtracting the upper layer momentum equation (2a) from the bottom one, then multiplying the result by $h_e\mathbf{u}^-$ yields the temporal evolution of the baroclinic energy:

$$\frac{1}{2}h_e\partial_t|\mathbf{u}^-|^2 + \frac{1}{2}g'\partial_t\eta_2^2 = -\nabla\cdot(h_e p^-\mathbf{u}^-) - \frac{h_2}{h}p^-\partial_t\eta_1 - p^-\mathbf{u}^+\frac{H_1}{h}\nabla b + LF^-, \quad (13)$$

where $h_e = H_1 h_2/h$ represents the total equivalent depth, $h_2 = H_2 - b, h = H_0 - b$ being the spatially-varying undisturbed fluid thicknesses for the bottom and the total layer respectively. The formulation of the two-layer SW in terms of perturbation elevations of the surface and interface around their resting position is powerful, as it makes the calculation of kinetic energy and available potential energy straightforward. The former characterizes the work needed to accelerate the fluid from rest to its stated velocity, the latter defines that portion of potential energy used to level the layer interface adiabatically away from its resting flat position. Hence, information about the energy cycle of the free least damped basin mode may be obtained from each of the work terms in equations (12) and (13). The integration of these terms over one oscillation period permits to address the energy routes of the flow perturbation, as well as its vertical conversion. The terms representing energy exchange between the different forms of potential and kinetic energy appear with opposite signs so they cancel one another out, as required, given that the system is energy-conserving in the inviscid limit.

We define the time average of any quantity $G(x, y, t)$ over the oscillation period T by

$$\overline{G} = \frac{1}{T}\int_0^T G(x, y, t')\,dt', \quad (14)$$

and the domain average by

$$< G > = \frac{1}{L_x L_y}\int_0^{L_x}\int_{-L_y/2}^{L_y/2} G\,dx\,dy. \quad (15)$$

The real physical solution being $\mathbf{u} = \Re(\hat{\mathbf{u}}\,e^{\omega t})$, the kinetic energy is obtained by multiplying the complex momentum equations by the complex conjugate of the velocity $\hat{\mathbf{u}}^*$ and then adding this to the product of the complex conjugate of this equation with $\hat{\mathbf{u}}$. The time evolution for the kinetic energy follows:

$$\Re(\omega)\left(\frac{1}{2}\hat{\mathbf{u}}^*\hat{\mathbf{u}}\right), \quad (16)$$

with $KE = \frac{1}{2}|\mathbf{u}^2|$ the perturbation kinetic energy per unit mass, and $\Re()$ indicates the real part. Similarly, the continuity equation expressed in terms of the vertical displacement of the interfaces is multiplied by the complex conjugate of the layer interface and added to the complex conjugate of this entire quantity, to obtain the time evolution for the available potential energy, following:

$$\Re(\omega)\left(\frac{1}{2}\hat{\eta}^*\hat{\eta}\right), \quad (17)$$

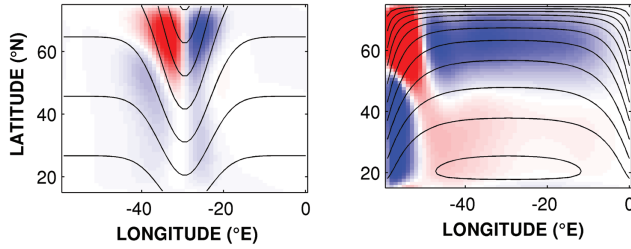with $APE = \frac{1}{2}\eta^2$ the perturbation available potential energy per unit mass.

Figure 7. Coupling mode term *PF* subject to Equation (18) in the two cases of bottom topography. Overlaid are the geostrophic contours f/h_2.

The time-rate-of-change of the perturbation total energy can be computed with (16) and (17), and the basin-integrated total energy budget (12) and (13) becomes:

$$\omega_r(\langle \overline{KE^+} \rangle + \langle \overline{APE^+} \rangle) = \quad \langle \frac{h_2}{h} \overline{p^- \omega_r \eta_1} \rangle + \langle \frac{H_1}{h} \overline{p^- \mathbf{u}^+ \nabla b} \rangle + LF^+,$$

$$\omega_r(\langle \overline{KE^-} \rangle + \langle \overline{APE^-} \rangle) = -\langle \frac{h_2}{h} \overline{p^- \omega_r \eta_1} \rangle - \langle \frac{H_1}{h} \overline{p^- \mathbf{u}^+ \nabla b} \rangle + LF^-. \qquad (18)$$

The first term on the rhs of (18) corresponds to the contribution of the free surface variation to the work of the pressure forces. This term is almost negligible, contributing less than one percent to the energy budget. This smallness justifies the rigid-lid approximation. The second term corresponds to the contribution of the bottom topography variation to the work of the pressure forces. This term, called *PF* hereafter, appears with an opposite sign in the vertical partition of the energy and allows for the energy conversion between the vertical modes with variable bottom topography. The source/sink work terms for the barotropic/baroclinic energy that occur in (18) then reduces to:

$$\begin{aligned}
PF &= \langle \tfrac{H_1}{h} \overline{p^- \mathbf{u}^+ \nabla b} \rangle &&= \langle \tfrac{H_1}{h} \overline{\Re(p^- u^{+*}) \nabla b} \rangle A, \\
LF^- &= \nu \langle \overline{h_e \mathbf{u}^- \nabla^2 \mathbf{u}^-} \rangle &&= \nu \langle h_e \Re(\mathbf{u}^- \nabla^2 \mathbf{u}^{-*}) \rangle A, \\
LF^+ &= \nu \langle \overline{\mathbf{u}^+ (H_1 \nabla^2 \mathbf{u_1} + h_2 \nabla^2 \mathbf{u_2}))} \rangle &&= \nu \langle \Re(\mathbf{u}^+ (H_1 \nabla^2 \mathbf{u_1^*} + h_2 \nabla^2 \mathbf{u_2^*})) \rangle A,
\end{aligned} \qquad (19)$$

in which $A = (e^{2\omega_r T} - 1)/2T$. In an ocean basin with variable topography and stratification, the work of the pressure forces in the fluid interior lead to an energetic attenuation of the baroclinic field by releasing the available potential energy. In a flat bottom ocean, the pressure forces cannot do work on the barotropic mode and the conversion is zero. In order to gain further insight into the coupling between the vertical modes, the term *PF* is shown in Figure 7.

For the simplest case of the ridge topography, the coupling acts as a sink (source) of baroclinic (barotropic) energy where the bottom slope is negative, that is on the eastern flank of the ridge, and a source (sink) where the bottom slope becomes positive, that is on its western flank. Overall, the sink of the baroclinic energy is greater than the source
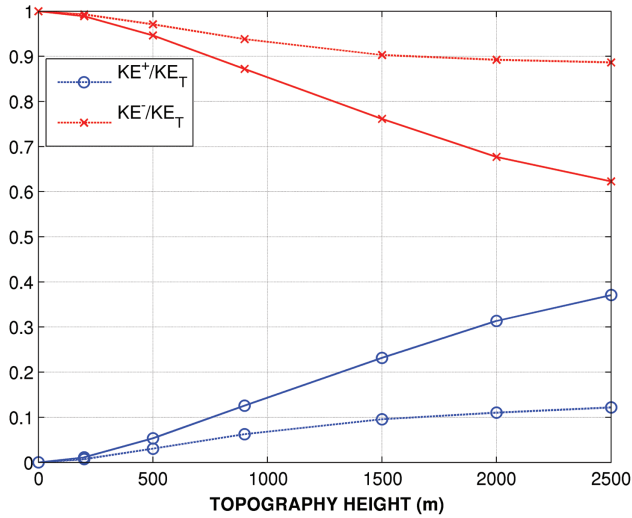
Figure 8. Vertical mode kinetic energy conversion (scaled by the total KE) of the least damped basin mode over the oscillation period as function of the topographic height. The dashed (solid) line corresponds to the MOR (CR) experiment, while the circle (cross) labels the barotropic (baroclinic) mode.

particularly in the CR-experiment, suggesting that the coupling term contributes to weaken the baroclinic mode by generating a barotropic circulation.

The amplitudes of the kinetic energy conversion in the different topographic experiments are shown in Figure 8. The resulting barotropic circulation is substantially sensitive to the form of topography: around 10% (25%) of the kinetic energy of the baroclinic mode is converted into barotropic mode under the effect of 1,500 m-high MOR (CR) topography, over one oscillation period.

The working terms contributions to the damping rate ω_r are identified by dividing each value in (19) by the total energy E to overcome the arbitrary amplitude of the mode. The box diagrams depicted in Figure 9 display the basin-integrated energy budgets for the least damped basin mode: they show the energy conversion between the reservoirs of available potential energy (APE), the barotropic kinetic energy (KE^+) and the baroclinic kinetic energy (KE^-) for the flat-bottom, MOR-bottom, and CR-bottom cases. The link between KE^+ and KE^- is provided by the pressure forces via the interaction with the APE reservoir through the work of the JEBAR term. In the MOR-bottom case, 90% of the KE^- of the system is dissipated by lateral friction and less than 10% is withdrawn and deposited in KE^+ under the pressure forces. It seems also that the energy flow along the pathway $KE^- \rightarrow APE \rightarrow KE^+$ is substantially stronger in the bowl-shaped topography experiment due to closed PV contours along which the energy conversion occurs more efficiently.
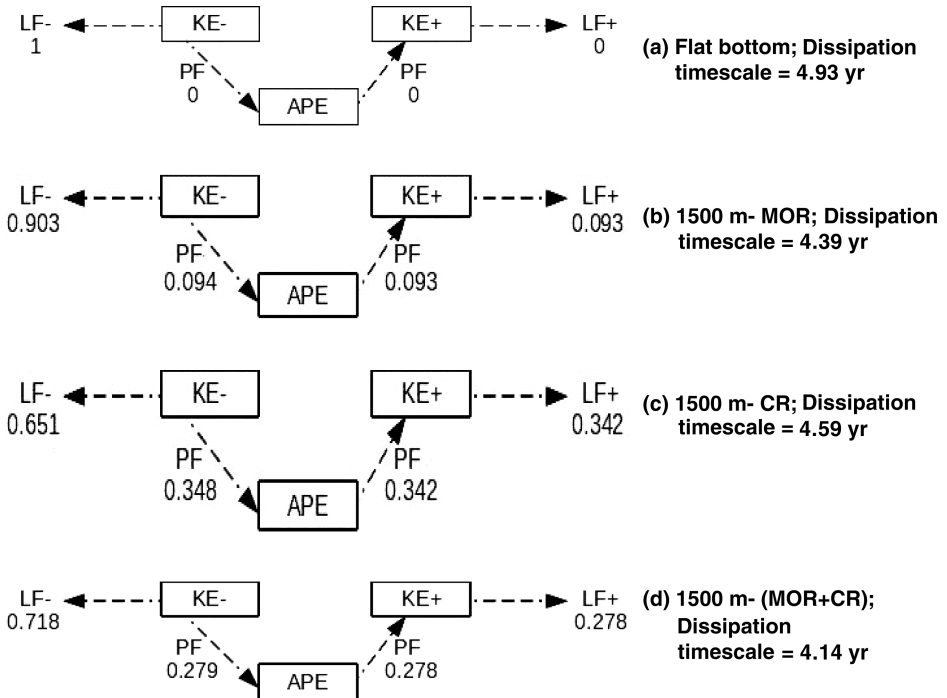
Figure 9. Perturbation energy box diagram showing the baroclinic total-drag energy route for the least damped basin mode. Energy budgets are evaluated after taking the volume integral in the global domain based on (18) as detailed in section 4.2. Energy conversion terms are normalized by ω_r. The direction of energy conversions are indicated by the arrows. Unbalanced budgets are due to numerical truncation errors.

From the above calculations, it is clear that in some instances the topographic conversion of the least damped baroclinic mode into barotropic circulation is more efficient with closed potential vorticity contours than with blocked contours at the boundaries. One reason could be that the structure of the mode is modified by the topography near the boundaries, such that the viscous dissipation of the cross-shore velocities along slanted Rossby wave crests is reduced in favor of a conversion into barotropic energy through the JEBAR work. Indeed, a fraction of the baroclinic energy propagating westward is converted into barotropic energy over a variable bottom topography, the other runs along the western boundary following closed PV contours. Thus, the mode experiences less frictional interaction with the boundary than the ones running into the coast following blocked PV contours at the boundary, as it is the case for the flat-bottom and the mid-ocean ridge. The damping rate of the baroclinic mode no longer stems only from the absorption of long Rossby waves in the western boundary layer due to the tilting of the wavefronts. The latter arises because of the differential phase speed, as it is the case for our flat bottom and MOR experiments, as well as the reduced

gravity of Cessi and Louazel (2001). Rather, the damping rate is also modulated by the shape of mean PV contours along the western boundary (CR topography case).

However, this argument becomes more subtle for a mixed topography taken to be the sum of the previous ones. To demonstrate this, we repeat the same calculations with a 1,500 m-[MOR + CR] bottom height and take a look at the energy transfer terms. The energy box diagram of the least damped basin mode shows a barotropic conversion of only 27.7% compared to 71.8% dissipated by lateral friction. This increase of dissipation by the small scale-selective harmonic friction term may be understood as a consequence of the enhanced topographic scattering of the flow into smaller scales.

Hence, the energy budget demonstrates the weak effect of topography through the vertical mode coupling under a catalyst of sloping bottom topography, compared to frictional processes on the thermal structure (i.e. the baroclinic response). This conclusion agrees fairly well with two-layer calculations of Anderson and Gill (1975) and the more realistic, though still linear, calculation of Bryan (1969).

5. Parameter sensitivity analysis

We have addressed the effect of topography on baroclinic unforced modes with a particular focus on the mechanisms affecting their decay. The potential effect of topography is the damping of the gravest baroclinic mode, as suggested in other works (e.g. Greatbatch et al. 1997; Winton 1997; Buckley et al. 2012). This damping is found to be sensitive to the form of the topographic features, although it remains smaller than the viscous decay at first order even with large amplitude topography.

Given the expense that investigating the linear stability analysis with a broad range of parameters would entail, we were limited to low resolution that required the use of an eddy coefficient unrealistically large to maintain the numerical stability and suppress accumulation of energy in the smallest unresolved scales. At higher resolution though, we wonder if our finding relative to the predominance of the viscous sink, with respect to the topographic dissipation remains relevant in the limit of weak friction. The issue then would be how to select the largest scale modes among numerous structures.

We consider successively the influence of a). additional layer thickness diffusion, b). a decrease of the eddy viscosity, and c). variation of the internal Rossby radius.

a. Sensitivity to dissipation parametrization

Because dissipative scale selection is the essential ingredient for the segregation of basin modes, it is important to verify that the results are robust to changes in the form of friction. To address this question, we proceed to an additional set of computations in which thickness diffusion $\lambda\nabla^2 h$ is appended in the continuity equation in order to investigate the behavior of the damping rate and oscillation period of the decadal variability in response to various dissipation parametrizations. We carried out linear stability analysis for the three bottom
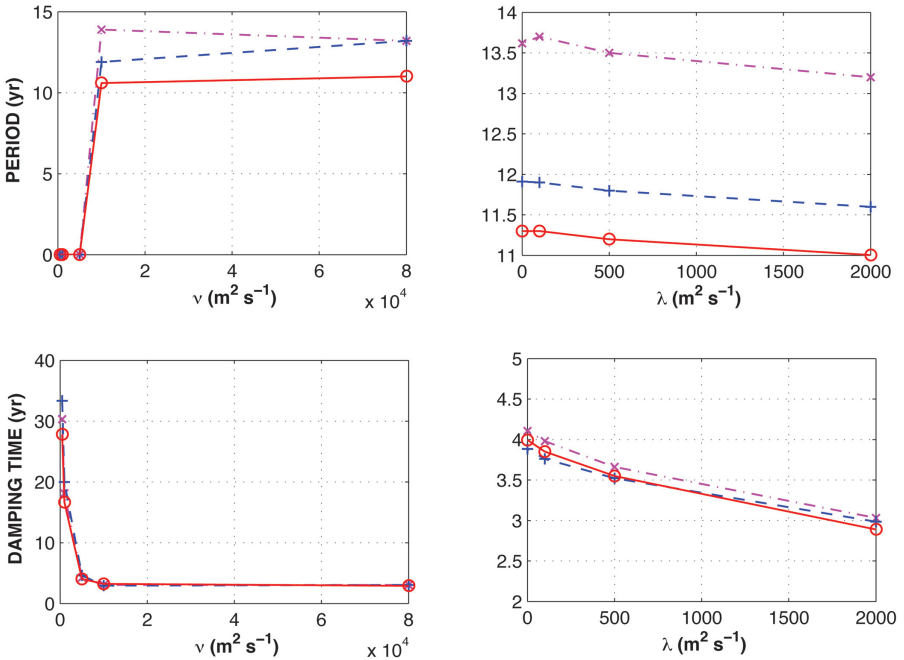
Figure 10. Sensitivity of the (top) oscillation period and (bottom) decay time (in years) to (left) horizontal viscosity ν for a fixed value of diffusivity $\lambda = 2 \times 10^3$ m^{2}s^{-1}, (right) horizontal diffusivity λ for a fixed viscosity $\nu = 10^4$ m^{2}s^{-1}, in the flat bottom (dash-dot cross line), the 1,500 m-MOR (solid plus sign line) and the 1,500 m-CR (solid circle line).

profiles (i.e. flat, MOR and CR) by using ν and λ as control parameters. In the first experiment, the horizontal eddy viscosity is decreased from 8×10^4 m^{2}s^{-1} down to 0 m^{2}s^{-1} while λ is kept fixed at 2×10^3 m^{2}s^{-1}. In the second experiment, ν is reduced to 10^4 m^{2}s^{-1}, while λ is gradually increased to test the possibility of replacing the initial strong friction with a moderate amount of viscosity and diffusivity. The decay time and period corresponding to the decadal variability for the two experiments are shown in Figure 10. Whatever the prescribed topography is, the horizontal eddy viscosity is found critical for the selection of the decadal period while the horizontal diffusivity only impacts the damping rate. Decreasing ν results in a more complex flow behavior, which might hamper the interpretation of the variability considerably. However, increasing the horizontal diffusivity λ only enhances the dissipation of the baroclinic variability.

A summary of all the experiments is depicted in Figure 11 in which one can follow the different branches of the least damped decadal mode eigenvalue in response to changing model parameters. This diagram confirms the weak effect of the topography with respect to frictional and diffusive processes. The diffusion appears more likely to affect the decay rate while the friction strongly monitors the oscillation period of the variability on decadal
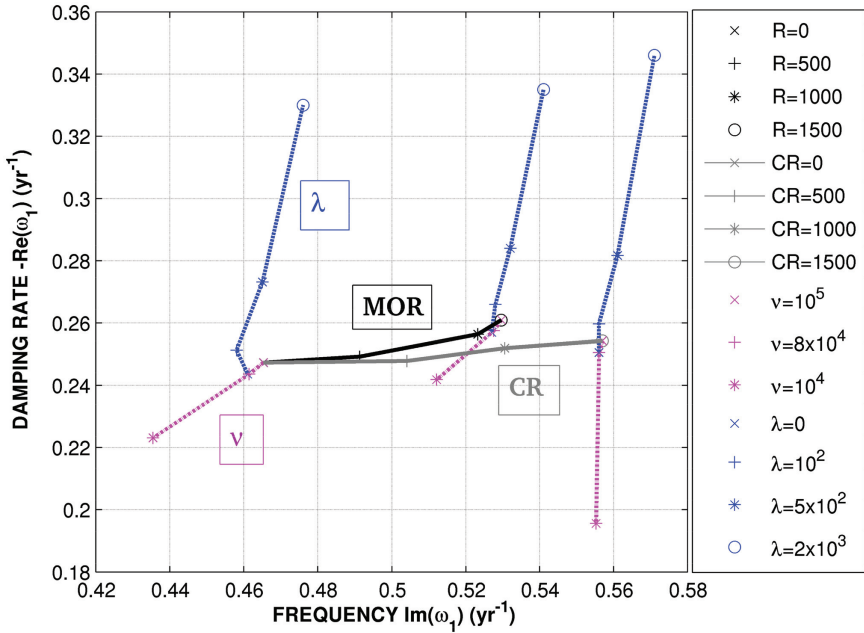
Figure 11. Sensitivity diagram in the $\omega_r - \omega_i$ plane for the least damped oscillation under different prescribed forms and amplitudes of topography and dissipation. The eigenvalue change under increasing (decreasing) diffusivity (viscosity) is dashed (dash-dotted). The solid black (gray) line indicates the effect of increasing MOR (CR) height.

timescales, at least in the case of coarse resolution. But does this still hold if the deformation radius is resolved?

b. Sensitivity to momentum dissipation

To clarify this point, we take a closer look at the effect of unresolved deformation Rossby radius on the behavior of the flat-bottomed basin mode patterns through a sensitivity experiment to friction. Specifically, the low-frequency least damped basin mode (corresponding to the largest real part eigenvalue) is therein tracked using its decay rate as a selection criterion while progressively decreasing the viscosity till the inviscid limit is reached. At this limit, the frequency of the least damped mode in the vicinity of inviscidness ($\nu = 10$ $m^2 s^{-1}$) is used as a selection criterion instead of its decay rate. In the ultra-low to low friction values, spurious modes prevent the capturing of the physical modes. The transition from the numerical regime to the physical regime does occur under a friction magnitude roughly corresponding to $O(\beta \Delta x^3)$ at which the numerical period coincides well with the reference proposed by Cessi and Louazel (2001) as the time it takes for the long Rossby wave to cross the basin along the northernmost boundary, $T_N = L_x/\beta R_d^2$ (Figure 12). For
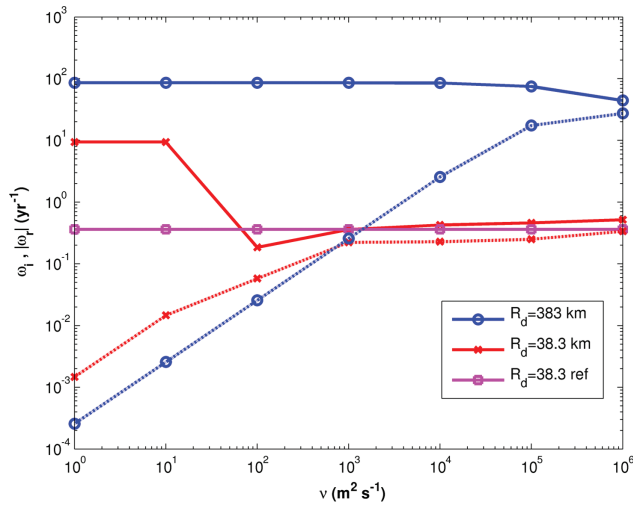
Figure 12. Least damped eigenmode frequency (solid line) and decay rate (dashed line) (yr^{-1}) as function of horizontal eddy viscosity ν in the flat bottom experiment. The red (blue) curve indicates the realistic (enhanced) stratification experiment. The magenta line corresponds to the reference frequency $2\pi/T_N$ of the realistic stratification experiment.

high viscosity values, the numerical period starts progressively to deviate from the reference as a result of the widening of the western boundary layer that reduces the zonal basin extent. This conclusion points out that the period of the least damped basin mode depends also on an "effective zonal basin extent" defined as $L_x - \delta_M$, rather than the geometric zonal basin extent, in a way similar to the effective northern boundary mechanism introduced by Yang and Liu (2003) for the establishment of the reference period in the shallow water framework. However, this high friction regime is completely irrelevant to the real ocean.

c. Sensitivity to internal deformation radius R_d

We repeat the same experiment, but for the case of a resolved deformation Rossby radius obtained by enhancing the stratification by two orders of magnitude. R_d is now ten times larger than the real value, but allows for an adequate resolution of motions on the scale of the Rossby radius of deformation without refining the horizontal model resolution. The reference oscillation period is then accordingly two orders of magnitude smaller. The results show that the period of the least damped basin mode remains constant with decreasing viscosity, in contrast to the realistic though unresolved R_d experiments where the decadal period is lost in the low friction regime (Figure 12).

Furthermore, large-scale structures do emerge in the inviscid limit (Figure 13) as well as at low and moderate viscosity values: this large-scale signal was spoiled by spurious (numerical) noise in the realistic stratification experiment when the viscosity was too low.
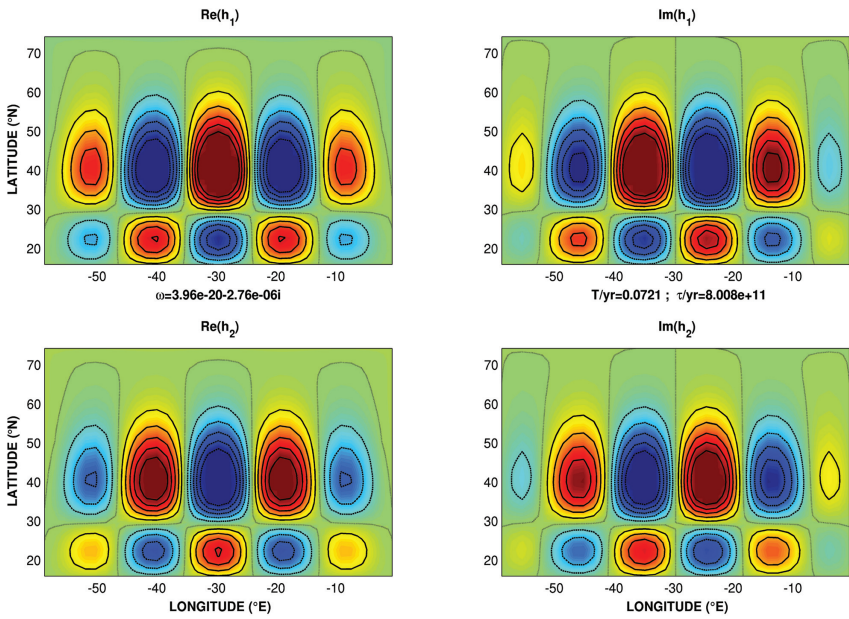
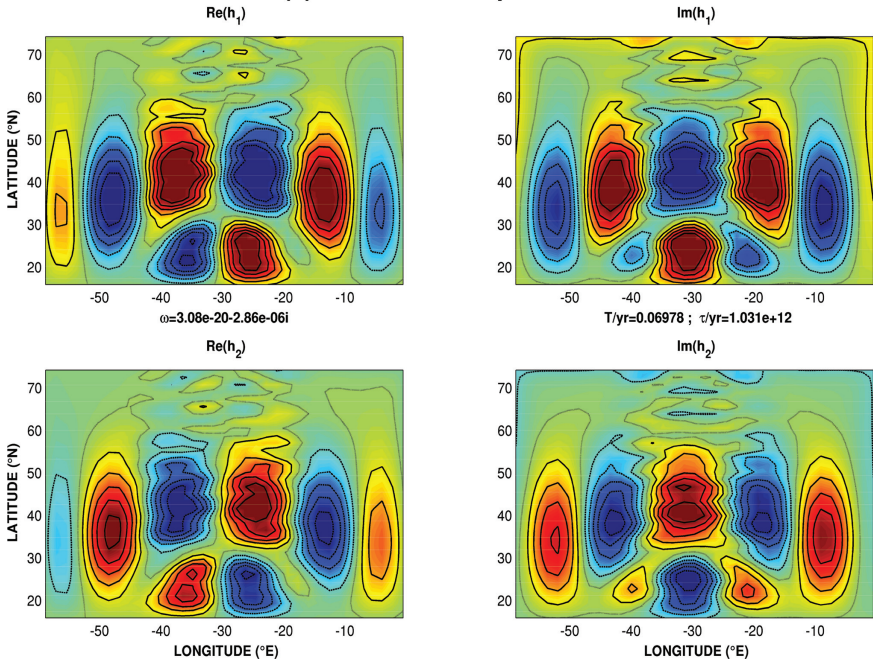Figure 13. Spatial pattern of the least damped mode in the inviscid limit ($\nu = 0$ m^2 s^{-1}) for the resolved Rossby radius experiment. The mode amplitude is arbitrary.

However, the structure of these modes differ noticeably from the initial baroclinic basin modes: the wavefront is no longer slanted but their amplitude tends to zero towards the eastern and western boundaries; the immediate consequence is that their damping rate is no longer set by their large-scale structure but decreases with momentum dissipation. This suggests that with higher horizontal resolution allowing to resolve the deformation radius, eddy viscosity would not be necessary to select the largest scale decadal modes.

In summary, the previous numerical experiments suggest that in some instances (i.e. in eddy-resolving models), explicit dissipation is actually not a necessary condition for selecting large scale basin modes. Large-scale, low-frequency modes emerge from the inviscid spectrum with the gradual addition of weak dissipation, and their structure is robust to the specific form of friction. It is then reassuring that under-resolving the deformation radius in a viscous basin does not alter the robustness of decadal basin modes. In response to a reviewer comment, we implemented other types of momentum dissipation, namely linear Rayleigh friction, and vertical eddy viscosity with linear bottom friction, instead of the Laplacian eddy viscosity. In the first case, the results were very similar, suggesting that the modal decay is independent of the type of momentum dissipation. In the latter case, the convergence of the eigenvalue computation only happens with rather large friction and viscosity coefficients.

6. Conclusion

We have analyzed the low-frequency, weakly dissipated basin modes in a two-layer ocean over a variable bottom topography. These large-scale modes with decadal periods are promoted through eddy viscosity at coarse resolution. The modes just described are the topographic analog of the reduced-gravity basin modes described by Cessi and Louazel (2001), Primeau (2002) and Yang and Liu (2003).

At midlatitudes, the gravest baroclinic mode is established through the transit of a mixture of Rossby and Kelvin waves during the geostrophic adjustment process. The frequency of the least damped mixed-wave mode scales as $2\pi/T_N$, where T_N is the long Rossby wave transit time along the northernmost boundary of a basin that does not feel the topography and falls near the decadal frequency. In the presence of topography, the period for the gravest basin mode is slightly shortened suggesting a net acceleration of long Rossby waves by bottom tops as pointed out by Tailleux and McWilliams (2000).

Through a systematic comparison of the results of various topographic features, the parameter sensitivity analysis enables us to determine which processes are critical to the variability. Changes in horizontal diffusion was shown to have no crucial influence on the gravest baroclinic mode of ocean variability. However, varying both amplitudes of viscous momentum dissipation and bottom topography exerted a leading damping role upon the baroclinic large-scale circulation. The build-up of a barotropic flow through the interaction of the flat-bottomed baroclinic mode with the prescribed topographic height is three times stronger in the case of continental rises, that constrain PV contours to close, than that

related to the mid-ocean ridge that imply blocked contours at the boundaries. However, the baroclinic energy decay through topographic vertical mode conversion remains smaller with respect to the viscous dissipation. Compared to the flat bottom case, changes in the eigenvalues remain lower than 10% in terms of the oscillation period and 20% for the damping time scale, even with large amplitude topography (up to 2,500 m height).

In contrast with our initial hypothesis, the broad message emerging from the present work suggests that the direct bottom topography damping on the basin modes is limited, and changes in the mean flows due to the topography may have more influence on the modes characteritics. It remains to be seen how the introduction of a mean flow, with the associated mesoscale dynamics, would interact with the bottom topography to excite or damp the large-scale decadal basin modes. We conjecture that large-scale stationary mean flow forcing (either by winds or heat fluxes) may well act to sustain the decadal mode (through large scale instability for instance) and to confirm the robustness of its signature, thus contributing to the decadal band of climate variability.

APPENDIX A

Barotropic transport budget

Starting with vertically integrating the momentum equation (2a) of the horizontal transport gives

$$\partial_t h\mathbf{u}^+ + f\mathbf{k} \times h\mathbf{u}^+ - \mathbf{u_1}\partial_t h_1 - \mathbf{u_2}\partial_t h_2 = -(H_1 + \eta_1 - \eta_2)\nabla p_1$$
$$- (H_2 + \eta_2 - b)\nabla p_2 + F^+. \qquad (20)$$

Knowing that $p_1 = g\eta_1$ and $p_2 = p_1 + g'\eta_2$, the pressure term in the rhs of (20) can be expressed as

$$-(H_1 + \eta_1)g\nabla\eta_1 - g'\eta_2\nabla\eta_2 - H_2\nabla p_2 + b\nabla p_2, \qquad (21)$$

which can be rewritten as:

$$-\nabla\left(H_1 p_1 + \frac{1}{2}g\eta_1^2 + \frac{1}{2}g'\eta_2^2 + H_2 p_2\right) + b\nabla p_2, \qquad (22)$$

Equation (20) now reduces to

$$\partial_t h\mathbf{u}^+ + f\mathbf{k} \times h\mathbf{u}^+ + N = -\nabla(H_0 p^+ + \chi) + b\nabla p_2 + F^+, \qquad (23)$$

in which the nonlinear term $N = \mathbf{u_1}\nabla \cdot (h_1\mathbf{u_1}) + \mathbf{u_2}\nabla \cdot (h_2\mathbf{u_2})$ represents the advection of perturbation thickness by the flow in each layer. Since $\eta_1 \ll \eta_2$, this term then reduces to

the effect of advection of interface anomaly by the baroclinic flow. This effect is assumed to be neglectable as long as the perturbation remains small compared to the undisturbed reference levels. The vertically integrated pressure gradient splits into three terms related to the barotropic pressure, the vertically integrated available potential energy $\chi = \frac{1}{2} g \eta_1^2 + \frac{1}{2} g' \eta_2^2$ and the bottom pressure. By neglecting the nonlinear term N before taking the curl of the depth-integrated momentum balance, the linear barotropic vorticity budget can then be derived as in Section 3.

APPENDIX B

Vertical mode energy partition

The barotropic motion equation is obtained by vertically integrating of the momentum balance:

$$\partial_t \mathbf{u}^+ + f \mathbf{k} \times \mathbf{u}^+ - \mathbf{u_1} \partial_t \left(\frac{h_1}{h} \right) - \mathbf{u_2} \partial_t \left(\frac{h_2}{h} \right) = -\nabla p^+ + p_1 \nabla \left(\frac{h_1}{h} \right) + p_2 \nabla \left(\frac{h_2}{h} \right) + F^+. \tag{24}$$

It gives after some simple algebraic manipulation:

$$\partial_t \mathbf{u}^+ + f \mathbf{k} \times \mathbf{u}^+ + M = -\nabla p^+ + \frac{p^-}{h} \left(h_2 \nabla \eta_1 - \nabla \eta_2 + \frac{h_1}{h} \nabla b \right) + F^+, \tag{25}$$

where $M = \mathbf{u}^- \partial_t \left(\frac{\eta_2}{\eta_1} \right)$ represents the advection of perturbation thickness ratio by the baroclinic flow similarly to term N in (23). It could then be neglected as long as the perturbation remains small compared to the undisturbed background state. For finite amplitude topography variations, low frequency, small waves, the leading order terms in (25) reduce to:

$$\partial_t \mathbf{u}^+ + f \mathbf{k} \times \mathbf{u}^+ = -\nabla p^+ + \frac{H_1}{h^2} p^- \nabla b + F^+. \tag{26}$$

Hence, the barotropic energy equation could then be derived by multiplying (26) by the depth-integrated horizontal transport $h \mathbf{u}^+$:

$$\frac{1}{2} h \partial_t \mathbf{u}^{+2} = -h \mathbf{u}^+ \nabla p^+ + p^- \mathbf{u}^+ \frac{H_1}{h} \nabla b + L F^+. \tag{27}$$

Enforcing the mass conservation of the depth-integrated horizontal transport

$$\partial_t \eta_1 = -\nabla \cdot (h \mathbf{u}^+), \tag{28}$$

and the expression of $p^+ = p_1 - \frac{h_2}{h} p^-$ in (27) gives:

$$\frac{1}{2} h \partial_t \mathbf{u}^{+2} + \frac{1}{2} g \partial_t \eta_1^2 = -\nabla \cdot (h \mathbf{u}^+ p^+) + \frac{h_2}{h} p^- \partial_t \eta_1 + p^- \mathbf{u}^+ \frac{H_1}{h} \nabla b + L F^+. \tag{29}$$

Similarly to (24), the equation of motion for the baroclinic mode is obtained by subtracting the momentum equation of the upper layer from that of the bottom layer:

$$\partial_t \mathbf{u}^- + f \mathbf{k} \times \mathbf{u}^- = -\nabla p^- + L F^-. \tag{30}$$

Multiplying (30) by $h_e\mathbf{u}^-$ gives the baroclinic energy equation:

$$\frac{1}{2}h_e\partial_t\mathbf{u}^{-2} = -h\mathbf{u}^-\nabla p^- + LF^-. \tag{31}$$

Further manipulating the first term in the rhs of (31), first by exploiting the mass conservation of the lower layer in which the bottom flow is replaced by its barotropic and baroclinic counterparts

$$\partial_t\eta_2 + \nabla\cdot(h_2\mathbf{u}^+) = \nabla\cdot(h_e\mathbf{u}^-), \tag{32}$$

and then by mean of (28) that gives $\nabla\cdot\mathbf{u}^+ = -\partial_t\eta_1/h + \mathbf{u}^+\nabla b/h$ yields:

$$\frac{1}{2}h_e\partial_t\mathbf{u}^{-2} + \frac{1}{2}\partial_t\eta_2^2 = -\nabla\cdot(h_e\mathbf{u}^-\,p^-) - \frac{h_2}{h}p^-\partial_t\eta_1 - p^-\mathbf{u}^+\frac{H_1}{h}\nabla b + LF^-. \tag{33}$$

Adding (29) and (33) gives the time-rate of change of the total energy of the model, whose basin-integrated form vanishes identically in the inviscid limit.

REFERENCES

Anderson, D.L.T. and A.E. Gill. 1975. Spin-up of a stratified ocean with applications to upwelling. Deep Sea Res, *22*, 583–596.

Barnier, B. 1998. A numerical study on the influence of the mid-atlantic ridge on nolinear first-mode baroclinic rossby waves generated by seasonal winds. J. Phys. Oceanogr., *18*, 417–433.

Ben Jelloul, M. and T. Huck. 2005. Low-frequency basin modes in a two-layer quasi-geostrophic model in the presence of a mean gyre flow. J. Phys. Oceanogr., *35*, 2167–2186.

Bryan, K. 1969. A numerical method for the study of the circulation of the world ocean. J. Comput. Phys., *4(3)*, 347–376.

Buckley, M. W., D. Ferreira, J. Campin, J. Marshall and R. Tulloch. 2012. On the relationship between decadal buoyancy anomalies and variability of the atlantic meridional overturning circulation. J. Climate, *25*, 8009–8030.

Böning, C. W. 1989. Influences of a rough bottom topography on flow kinematics in an eddy-resolving circulation model. J. Phys. Oceanogr., *19*, 77–97.

Cessi, P. and S. Louazel. 2001. Decadal oceanic response to stochastic wind forcing. J. Phys. Oceanogr., *31*, 3020–3029.

Cessi, P. and F. Primeau. 2001. Dissipative selection oflow frequency modes in a reduced-gravity basin. J. Phys. Oceanogr., *31*, 127-137.

Delworth, T. L. and coauthors. 2006. GFDL's CM2 Global Coupled Climate Models. Part I: Formulation and Simulation Characteristics. J. Climate, *19*, 643-674.

Gill, A. E., S. A. Green and A. J. Simmons. 1974. Energy partition in the large-scale ocean circulation production of mid-ocean eddies. Deep Sea Res., *21*, 499–528.

Greatbatch, R. J., K. A. Peterson and H. Roth. 1997. Interdecadal variability in a coarse resolution model with north atlantic bottom topography. Technical Report, Department of Oceanography, Dalhousie University, Halifax, Nova Scotia, Canada.

Herbette, S., Y. Morel and M. Arhan. 2003. Erosion of a surface vortex by a seamount. J. Phys. Oceanogr., *33*, 1664–1679.

Holland, W. R. 1978. The role of mesoscale eddies in the general circulation of the ocean-numerical experiments using a wind-driven quasigeostrophic model. J. Phys. Oceanogr., *8*, 363–392.

Huck, T. and G. K. Vallis. 2001. Linear stability analysis of the three-dimensional thermally-driven ocean circulation: application to interdecadal oscillations. Tellus, *53A(4)*, 526–545.

Huck, T., A. J. Weaver, and A. Colin de Verdière. 1999. On the influence of the parameterization of lateral boundary layers on the thermohaline circulation in coarse-resolution ocean models. J. Mar. Res., *57*, 387–426.

Kerr, R. A. 2000. A north atlantic climate pacemaker for the centuries. Science, *288*, 1984–1986.

LaCasce, J. H. 2000. Baroclinic rossby waves in a square basin. J. Phys. Oceanogr., *30*, 3161–3178.

LaCasce, J. H. and J. Pedlosky. 2002. Baroclinic rossby waves in irregular basins. J. Phys. Oceanogr., *32*, 2828–2847.

Lehoucq, R. B., D. C. Sorensen and C. Yang. 1996. ARPACK user's guide. Solutions oflarge scale eigenvalue problems with Implicitly Restarted Arnoldi Methods. SIAM, page 160p. URL http://caam.rice.edu/software/ARPACK/.

Liu, Z. 2003. Tropical ocean decadal variability and resonance of planetary wave basin modes. part i: Theory. J. Climate, *16*, 1539–1550.

Mellor, G., C. Mechoso and E. Keto. 1982. A diagnostic calculation of the atlantic ocean. Deep SeaRes., *29*, 1171–1192.

Mertz, G. and D. G. Wright. 1992. Interpretations of the JEBAR Term. J. Phys. Oceanogr., *22*, 301–305.

Primeau, F. W. 2002. Long rossby wave basin-crossing time and the resonance of low-frequency basin modes. J. Phys. Oceanogr., *32*, 2652–2665.

Rhines, B. P. 1977. The dynamics of unsteadycurrents, V. 6. The Sea, E. A. Goldberg, I. N. McCane, J. J. O Brien, and J. H. Steele, Eds., J. Wiley and Sons, 189–318, pp.

Rhines, P. B. 1969a. Slow oscillations in an ocean of varying depth. part 1. abrupt topography. J. Fluid Mech., *37*, 161–189.

Rhines, P. B. 1969b. Slow oscillations in an ocean of varying depth. Part 1. islands and seamounts. J. Fluid Mech., *37*, 191–205.

Ripa, P. 1978. Normal rossby modes of a closed basin with topography. J. Geosphys. Res., *83*, 1947–1957.

Sarkisyan, A. S. and V. F. Ivanov. 1971. Joint effect of baroclinicity and bottom relief as an important factor in the dynamics of sea currents. Izv. Acad. Sci. USSR Atmos. Oceanic Phys. (Engl. Transl.), *7*, 173–178.

Solomon, A., L. Goddard, A. Kumar, J. Carton, C. Deser, I. Fukumori, A.M. Greene, G. Hegerl, B. Kirtman, Y. Kushnir, M. Newman, D. Smith, D. Vimont, T. Delworth, G.A. Meehl and T. Stockdale. 2011. Distinguishing the roles of natural and anthropogenically forced decadal climate variability. Bull. Amer. Meteor. Soc., *92*, 141–156.

Spydell, M. and P. Cessi. 2003. Baroclinic modes in a two-layer basin. J. Phys. Oceanogr., *33*, 610–622.

Tailleux, R. and J. McWilliams. 2000. Acceleration, creation, and depletion of wind-driven baroclinic rossby waves over an ocean ridge. J. Phys. Oceanogr., *30*, 2186–2213.

Verron, J. and C. Le Provost. 1985. A numerical study of quasi-geostrophic flow over isolated topography. J. Fluid Mech., *154*, 231–252.

Winton, M. 1997. The damping effect ofbottom topography on internal decadal-scale oscillations of the thermohaline circulation. J. Phys. Oceanogr., *27*, 203–208.

Yang, H. and Z. Liu. 2003. Basin modes in tropical-extratropical basin. J. Phys. Oceanogr., *33*, 2751–2763.